JOM Journal of Optical Microsystems

RESEARCH PAPER

Portable single-beam cesium zero-field magnetometer for magnetocardiography

Rach Dawson,[a,*] Carolyn O'Dwyer,[a] Marcin S. Mrozowski,[a] Edward Irwin,[a] James P. McGilligan,[a] David P. Burt,[b] Dominic Hunter,[a] Stuart Ingleby,[a] Molly Rea,[c] Niall Holmes,[c,d] Matthew J. Brookes,[c,d] Paul. F. Griffin,[a] and Erling Riis[a]

[a]University of Strathclyde, Department of Physics, SUPA, Glasgow, United Kingdom
[b]University of Glasgow, Kelvin Nanotechnology, Glasgow, United Kingdom
[c]University of Nottingham, Sir Peter Mansfield Imaging Centre, University Park, Nottingham, United Kingdom
[d]Cerca Magnetics Limited, Nottingham, United Kingdom

ABSTRACT. Optically pumped magnetometers (OPMs) are becoming common in the realm of biomagnetic measurements. We discuss the development of a prototype zero-field cesium portable OPM and its miniaturized components. Zero-field sensors operate in a very low static magnetic field environment and exploit physical effects in this regime. OPMs of this type are extremely sensitive to small magnetic fields, but they bring specific challenges to component design, material choice, and current routing. The miniaturized cesium atomic vapor cell within this sensor has been produced through integrated microfabrication techniques. The cell must be heated to 120°C for effective sensing, while the sensor external faces must be skin safe ≤40°C making it suitable for use in biomagnetic measurements. We demonstrate a heating system that results in a stable outer package temperature of 36°C after 1.5 h of 120°C cell heating. This relatively cool package temperature enables safe operation on human subjects which is particularly important in the use of multi-sensor arrays. Biplanar printed circuit board coils are presented that produce a reliable homogeneous field along three axes, compensating residual fields and occupying only a small volume within the sensor. The performance of the prototype portable sensor is characterized through a measured sensitivity of 90 fT/$\sqrt{\text{Hz}}$ in the 5 to 20 Hz frequency band and demonstrated through the measurement of a cardiac magnetic signal.

Keywords: microfabricated; micro-electromechanical systems; optically pumped magnetometry; biomagnetism; systems integration; photonics

Paper 23014G received Jun. 23, 2023; revised Oct. 20, 2023; accepted Oct. 24, 2023; published Nov. 14, 2023.

1 Introduction

Measurements of magnetic fields generated by the human body provide a critical diagnostic and research tool.[1] Biomagnetic field measurements are noncontact and provide better spatial resolution than measurements of the electric component of a given signal, which is well attenuated by skin and tissue.[2] In addition, muscle movement can induce electrical artifacts and interference in the electrical signal, which may obscure signals of interest.[3]

Biomagnetic signal amplitudes are 6 to 10 orders of magnitude smaller than the earth's magnetic field of 50 μT, e.g., cardiac signals (~100 pT) and neural activity (between 10 and

*Address all correspondence to Rach Dawson, rach.dawson@strath.ac.uk

500 fT). Superconducting quantum interference devices (SQUIDs) demonstrate excellent sensitivity (~1 fT)[4] and for many years have been the primary tool for magnetoencephalography (MEG) measurements. However, SQUIDs require cryogenic cooling which places a limit on the size of the device and fixes the location of the sensors with respect to the head. Advances in optically pumped magnetometers (OPMs)[5–8] have led to demonstrations of sensors that approach the sensitivity of SQUIDs, while providing new measurement modalities[9] due to their size and portability. Zero-field OPMs do not require cryogenic cooling, and the relative simplicity of the sensor design lends the sensor to miniaturization, demonstrated by the availability and widespread use of several commercial sensors.[9,10] Due to miniaturization OPMs can be placed within just millimeters of the scalp surface. As such, theoretical gains in source reconstruction accuracy can be achieved in MEG due to an ability to better sample the neuromagnetic field.[11–14]

The OPM described herein utilizes the Hanle effect to detect magnetic signals.[15] This principle describes the effect of an atomic vapor on the absorption of laser light when the atoms experience a magnetic field. The atomic vapor is pumped and probed using a single laser beam, and the change of the light absorption is detected through an on-board photodiode (PD). The transmission of laser light is at a maximum when the atoms experience zero-field in three axes. The response of the light transmission in the presence of non-zero fields exhibits a Lorentzian distribution on the axes transverse to the laser beam. Magnetic field modulation is applied to the atoms to detect the quadrature demodulated signal along the transverse axes.

The atomic vapor cell contains a vapor of cesium as the sensing atom. Micro-electro-mechanical systems (MEMS) fabrication techniques[16,17] have been used to manufacture this alkali vapor cell. These techniques create a very compact vapor cell with outer dimensions $10 \times 10 \times 4$ mm^3, whose optical access allows it to reside in a planar stack of components along the optical path of the laser beam. Since the measured magnetic field decays as an inverse function of the distance cubed,[18,19] it is advantageous to place the sensor in close proximity to the signal source, with sensor to skin contact therefore being highly desirable. OPMs using alkali vapor must create a sufficient density of atoms in order to operate in the spin-exchange relaxation free (SERF) regime. As a result, the atomic vapor cell must be heated to achieve a vapor density of $\simeq 10^{14}$ cm^{-3}. The surface temperature of the sensor package is of great importance, especially when many sensors are operated in an array around the head, as in MEG. Here, the sensor must also be capable of operating next to participants' skin to take biomagnetic measurements, while maintaining high thermal uniformity across the cell. The typical skin-safe temperature defined by the US FDA is a maximum of 40°C. In the sensor described herein, the decision to use cesium as the sensing atom was informed by the expected operating temperature required to achieve optimal sensitivity, which is ≃30°C lower than that of rubidium.[20,21] Furthermore, cesium has a well-demonstrated suitability in the field of biomagnetic sensing.[22] Careful selection of the sensing atom to inform skin-safe sensor operation temperature is similarly demonstrated by room-temperature helium zero-field sensors.[23]

OPMs of the type described here must operate close to zero-field. Typically much of the Earth's field is attenuated using shielding, such as a magnetically shielded room (MSR), which is commonly used for biomagnetic measurements in hospitals and research institutes. Approximately 10 to 50 nT of residual field remains in even high specification MSRs.[24] The remaining environmental magnetic fields can be compensated within the sensor package using coil pairs that act on each axis.

This article will cover the design, development, and testing of a cesium portable zero-field OPM.

2 Methods

2.1 Sensor Design

The topology of the prototype cesium portable sensor configuration is presented in Fig. 1(a). The sensor head is enclosed in a five-layer mu-metal shield during development and testing, though due to its size and portability, it may be easily moved to an MSR. Laser light from a distributed Bragg reflector (DBR) laser tuned to the cesium D_1 line, 895 nm, is delivered to the sensor head via an optical fiber. The fiber-coupling port is labeled as FC and fits a non-magnetic fiber collimator (Schäfter Kirchhoff 60FC-4-M12-10-Ti).

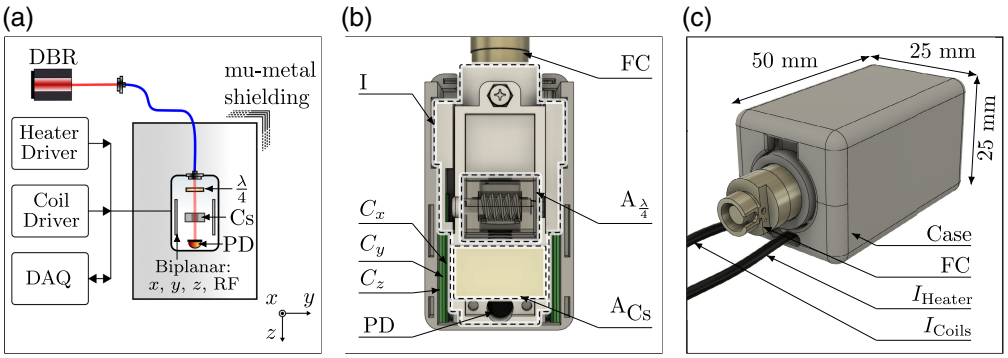

Fig. 1 (a) Topology of the sensor configuration. The sensor-head operates inside a five-layer mu-metal shield. The laser light from the DBR is delivered to the sensor-head using an optical fiber. The driving and control electronics including DAQ unit, coil driver,[25] and cell heater operate outside the shielding. Driving and detection signals are brought to the sensor-head on a cable bundle of individually shielded twisted pairs. (b) CAD model (top-view) of the sensor head. I, Insert containing optics and vapor cell; C_x, C_y, C_z, bi-planar coils for uniform magnetic field control across each axis; PD, photodiode, for detection of the light after it passes through the cell; A_{Cs}, vapor cell oven assembly, containing cesium vapor cell, heating resistor, and insulation; $A_{\frac{\lambda}{4}}$, adjustable quarter-waveplate; FC, non-magnetic FC with collimating lens. (c) CAD model of the external faces of the sensor package. Case: 3D printed external package casing; I_{Heater}, shielded cable for heating currents; I_{Coils}, shielded cable for coil currents and PD signal.

To compensate for stray fields experienced by the cell, electromagnetic coils are placed within the sensor package to generate fields in three cartesian directions. It is of critical importance that the current does not generate excess magnetic field noise, which would degrade the sensitivity of the sensor. These coils are driven using a custom low noise current driver[25] with a current range allowing compensation of fields up to 1500 nT on each axis. The current noise on this driver is in the nA regime, leading to a maximum of 28 $\mathrm{fT}/\sqrt{\mathrm{Hz}}$ contribution in magnetic noise over the frequency range of interest of the sensor.

The plan-view diagram of the sensor head in Fig. 1(b) shows several key components. The optical components are housed in a three-dimensional (3D)-printed optical insert, I, which locates the vapor cell, fiber coupler (FC), and PD. The optical insert allows for consistent alignment of optical components precisely with respect to the 5 mm diameter optical path through the sensor. The PD is included for detection of the light after it passes through the cell. The PD output is amplified through a custom transimpedence amplifier with a gain of 5000 V/A.

The external-view diagram of the sensor head in Fig. 1(c) shows the 3D printed sensor case with external dimensions of $25 \times 25 \times 50$ mm^3. The interfacing cables for the heater current (I_{Heater}) and coil currents (I_{Coils}) are indicated with reference to the sensor package.

2.1.1 *Cell heating assembly*

At the core of the portable sensor is an MEMS fabricated silicon cell (external dimensions $10 \times 10 \times 4$ mm^3), with 3 mm of silicon anodically bonded between two layers of 0.5 mm borofloat glass, resulting in a 3 mm optical path length and 6×6 mm^2 optical aperture, shown in Fig. 2(a). The cell contains a vapor of cesium and nitrogen (N_2) buffer gas, which has been achieved by depositing cesium azide (CsN_3) in the vapor cell before the final glass bond is made in a nitrogen environment. After sealing, the cesium azide is dissociated using UV light. The resultant composition is saturated cesium vapor and 225 Torr of N_2. The presence of N_2 suppresses the rate of wall collisions and extends the lifetime of the atomic coherences by altering the mean free path of the alkali atoms, making their effective motion diffusive rather than ballistic with respect to the cell.[26]

For optimal sensitivity, the sensor must operate in the SERF regime which is achieved through heating of the atoms to a sufficiently high atomic density to suppress the effect of spin-exchange relaxation. Typical atomic vapor densities to achieve the SERF regime are $\simeq 10^{14}$ cm^{-3}, which in cesium corresponds to 100 to 120°C for the cell volume discussed herein.[7,21,27,28]

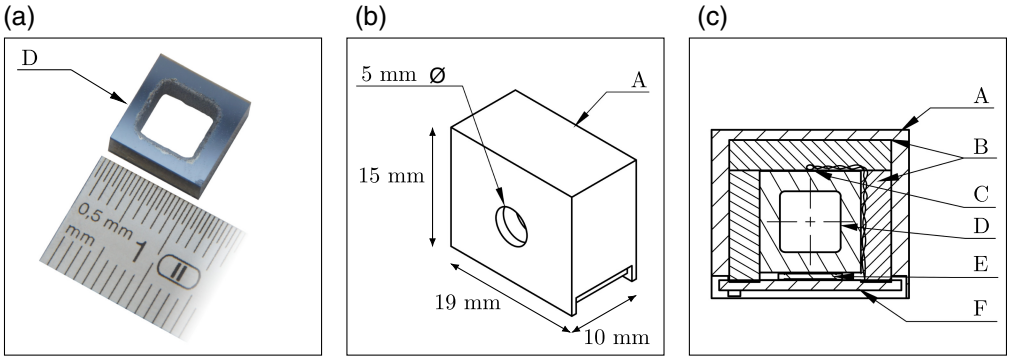

Fig. 2 Design of cesium MEMS cell and heating assembly. (a) Photograph of cesium MEMS cell with 3 mm optical path. (b) Drawing of the external cell oven assembly. (c) Cross-section of oven, insulation and cell. A: 3D printed cell housing, B: calcium-magnesium silicate thermal insulation, C: t-type thermocouple, D: cesium 3 mm MEMS cell, E: non-inductive SMD resistor, F: heater interface PCB.

The vapor cell is heated ohmically through direct contact with an aluminum nitride non-magnetic thin-film resistor (PN: PCNM2512K8R20FST5) as a heating element [Fig. 2(c)], thermally bonded to the MEMS cell surface using boron nitrate paste and driven by a high efficiency AC driver at 274.699 kHz, a frequency chosen to be far outside the bandwidth of the sensor, and at a non-integer multiple of the mains line frequency (50 Hz). The heating element covers a total heating surface area of 20.2 mm^2 equating to 67% coverage of the MEMS cell bottom-edge surface and resulting in rapid heating. The heater driver has been measured to be 95% efficient at an input power of 1 W to achieve a temperature of 120°C.

The vapor cell is insulated with calcium-magnesium silicate thermal insulating sheets (3 mm thick) across all faces and housed in a 3D printed enclosure to create an insulated oven [Fig. 2(b)]. The printed enclosure is manufactured using a Formlabs printer in high-temperature V2 resin with a heat deflection temperature of 238°C at 0.45 MPa, ensuring that even at an operating temperature of 120°C, the oven will not deform. Closed-loop temperature feedback allows for stable heating, using a non-magnetic T-type thermocouple mounted to the top of the cell [Fig. 2(c)] for temperature monitoring and a proportional-integral-derivative (PID) controller for temperature control. The distance from the sensing area inside the cell to the outside of the package measures 12 mm.

2.1.2 *Coil design*

Multi-axis magnetic field control may be achieved using bi-planar coils, coil-pairs which are oriented in two parallel planes. As such, bi-planar coils occupy a smaller footprint than a traditional Helmholtz design. Bi-planar coils have been utilized in zero-field sensing within an OPM sensor package[29] and external to the sensor through active field control inside MSRs.[24]

Here, the sensor requires three-axis control of the magnetic field in the region of the cell to maintain a zero-field environment. The coils described here are designed as a custom component for assembly within the sensor package to occupy as small a footprint within the sensor as possible without obscuring the beam path. Figure 3(a) shows all three bi-planar coils with respect to the caesium MEMS cell and a defined sensing area (shaded square), where red and blue indicate opposing current directions, either clockwise or anti-clockwise. Each coil pair is positioned symmetrically about the sensing area. Figure 3(b) shows the direction (indicated by the vector arrow) of the homogeneous magnetic field produced by each coil (C_x, C_z, and C_y) across the sensing area (in purple), between a coil pair separated by distance S across the xz-plane.

The design of bi-planar coils is computationally complex. bfieldtools[30,31] is a python package that facilitates bi-planar coil design through a well defined process.[29] This package can be used to define current loops that produce a magnetic field in the desired direction across a specified sensing region, chosen to be $8 \times 8 \times 8$ mm^3. The sensing region defined here is larger than the real sensing volume within the vapor cell in order to ensure homogeneity.

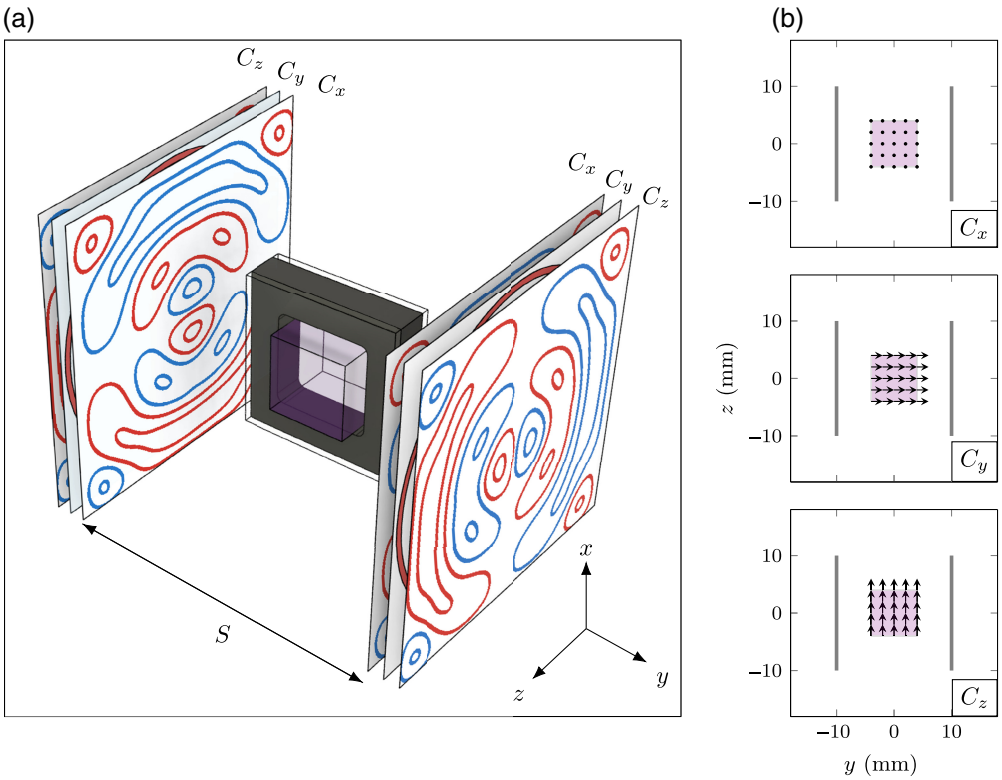

Fig. 3 Coil pairs C_x, C_y, and C_z apply homogeneous fields across the x, y, and z axes, respectively. Each coil pair is separated by distance $S = 20$ mm, red and blue indicate opposing current directions. Coils are designed for a defined homogeneous sensing region (shown in purple) centered between the coils which requires high homogeneity throughout. (a) All three coil pairs located with respect to caesium MEMS cell (external dimensions, $11 \times 11 \times 5$ mm^3). (b) Top-down view of the sensing region showing the magnetic field direction (vector arrows) for each coil pair. Coil pair location is indicated by gray lines.

Here, bfieldtools is used to create the coils C_x and C_z, and a Helmholtz configuration is used for C_y due to computational ease.

The homogeneity of the magnetic field produced across the sensing region for each coil design (C_x, C_y, and C_z) is modeled to verify the coil design suitability. Printed circuit boards (PCBs) are designed for each coil in KiCAD, in accordance with PCB design practices[29] and manufacturer tolerances. The PCB magnetic field coils have been designed such that the leakage field is attenuated to <5% of the applied field at a distance of 20 mm from the package outer, which aligns well with common spacing of OPM sensor arrays for MCG.[32,33]

Three-axis field control of the portable cesium sensor is achieved through bi-planar coils shown in Fig. 4. Each axis has a unique coil design C_x, C_y, and C_z, which is designed to operate as a symmetric pair which sits on the xz-plane of the portable sensor, either side of the MEMS cell. Figure 4(b), 4(e), and 4(h) show the modeled magnetic field homogeneity across the full region between the coil pairs on the xz-plane, where the sensing region (MEMS cell) is highlighted in purple.

From the current contours, an individual PCB is designed for each coil pair, with the coil contained within a 20×20 mm area on the PCB. Each coil design is manufactured on a 0.4 mm thick two-layer PCB. The coil pairs are installed in the portable sensor package in a configuration where three coils are stacked on each side of the sensor. Wire routing between corresponding coil pairs is achieved through manual wiring of 26 AWG twisted wire pairs. The expected magnetic field and homogeneity of PCB coils is confirmed through calibration by comparison of the measured magnetic resonance (through sweeping the magnetic field across one axis) with a well-calibrated external set of coils, which themselves have been characterized by a total-field OPM to <1% precision. All coils produced fields within 1% of expected calculated values, see Table 1 while showing no indication of mutual inductance.

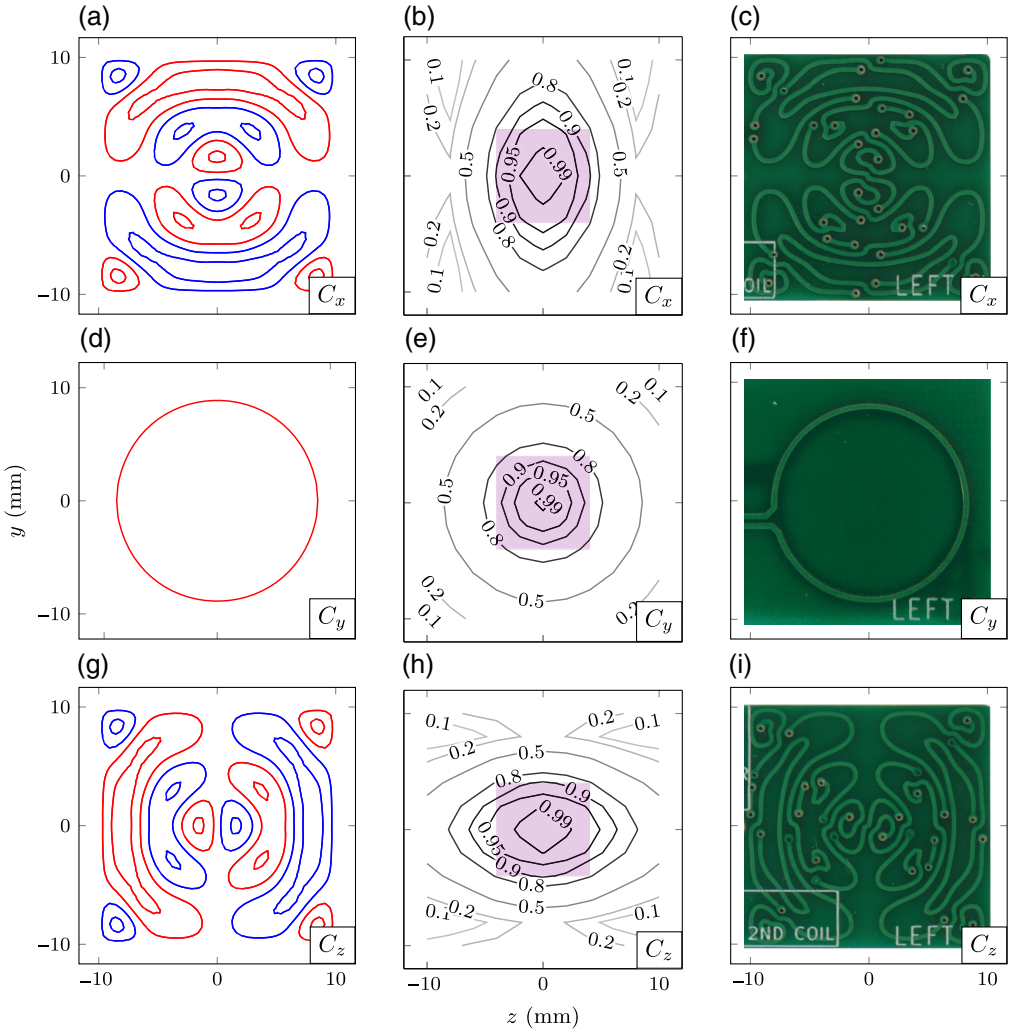

Fig. 4 Symmetrical three-axis bi-planar coils assembled across the *xz*-plane of the portable sensor. Each axis (*x*, *y*, and *z*) has a respective unique coil design C_x, C_y, and C_z, indicated in each subplot. (a), (d), (g) bfieldtools current contours produced for the specified desired field, red and blue indicate opposing current directions. (b), (e), (h) Modeled magnetic field homogeneity calculated across the full region between coil pairs, with sensing regions highlighted in purple. (c), (f), (i) Photograph of manufactured PCB designed based on bfieldtools current loops shown in (a), (d), (g).

Table 1 Biplanar coil field to current ratios. Axis: direction of B-field. Expected: modeled field-to-current ratio (nT/mA) from bfieldtools for *x*- and *z*-axis and from Helmholtz calculation for *y*-axis. Measured: experimentally measured field-to-current ratio (nT/mA) using the well-calibrated SERF OPM. Homogeneity (%): average deviation across the sensing region with respect to the expected field-to-current ratio.

Axis	Expected (nT/mA)	Measured (nT/mA)	Homogeneity (%)
x	9	9.0	≃93
y	12	11.9	≃88
z	9	9.0	≃93

2.1.3 *Adjustable waveplate*

The optimum light polarization for a given OPM depends on a number of operational factors that form a complex set of optical pumping dynamics. The optimum light polarization was not known *a priori* for the prototype described here and as a result, this polarization must remain adjustable

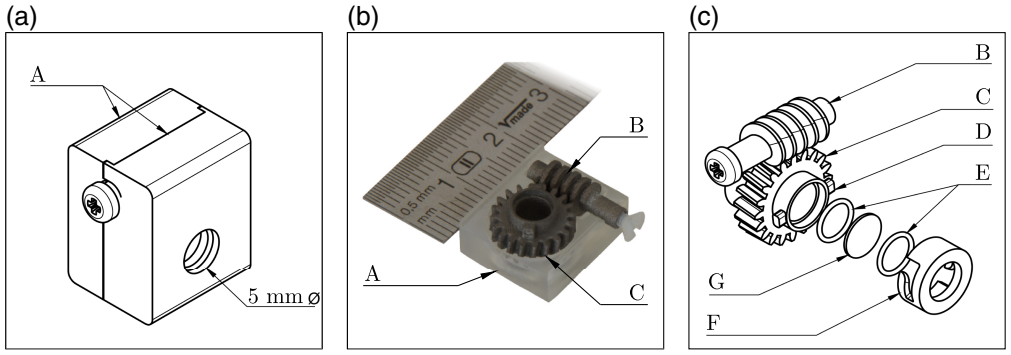

Fig. 5 Design of adjustable quarter-waveplate ($A_{\frac{\lambda}{4}}$) (a) isometric, (b) cross-sectional, and (c) exploded views. (b) Photograph of the titanium printed rotating waveplate mechanism. A: 3D printed enclosure consisting of two push-fit parts with external dimensions ($17 \times 14 \times 12$ mm). B: Worm drive gear. C: Worm gear where $n_2 = 20$ and external diameter = 10 mm. D: Locating extrusions for retention cap. E: 5.2 mm diameter O-rings. G: 5 mm diameter quarter-waveplate. F: Waveplate retention cap.

until other operational parameters are fixed. Here, we introduce an adjustable rotating quarter-waveplate design ($A_{\frac{\lambda}{4}}$) that provides adjustment of light polarization before the light is incident on the atoms.

Typically, single-beam zero-field sensors require a circular component of polarization for efficient optical pumping. Experimentally, we have found that the sensor signal is maximized through the use of elliptically polarized light,[34] whose ellipticity is chosen to maximize the magnetic resonance amplitude. Here, a quarter-waveplate is used to convert linearly polarized light from the fiber to elliptically polarize light before passing through the MEMS cell.

To achieve rotation, a geared mechanism is utilized. The selection of the gear type depends on the required configuration of the drive gear and driven gear. In this use-case, access to any rotation mechanism once inside the sensor package is constrained to only be at 90 deg to the driving gear. Worm gears are most suited to this orientation and provide high rotation precision for a small footprint. Gear ratio i quantifies the resolution or precision of the rotation and is defined by the number of gear teeth of the worm gear, n_1, and the number of helical threads that span the length of the shaft of the worm drive gear, n_2, where $i = \frac{n_1}{n_2}$.

Figure 5 shows the full adjustable quarter-waveplate design ($A_{\frac{\lambda}{4}}$). Here, the waveplate is a 5 mm diameter quarter-waveplate. Figure 5(b) shows the worm drive gear, which has a single helical thread such that one turn of the worm drive causes an advance of one tooth of the worm gear, $n_2 = 1$, controlled through the turning of a nylon screw embedded along its length. The worm gear is a 20 toothed gear, $n_1 = 20$, with an external diameter of 10 mm. The subsequent gear ratio, $i = 20:1$, equates to five turns of the worm drive to give a $\pi/2$ retardation, moving from fully linear to fully circular polarisation.

Figure 5(a) shows external faces of rotating quarter-waveplate assembly with total external dimensions of $17 \times 14 \times 12$ mm. The enclosure for all rotating components consists of two push-fit parts. In Fig. 5(c), all internal components can be seen, exploded along the optical axis. The waveplate and gears must be insensitive to movement as vibration of the waveplate can couple as polarization noise into the sensing atoms. To dampen vibration, two O-rings (5.2 mm external diameter) are used to sandwich the quarter-waveplate into an internal ledge carved into the worm gear, this is all secured by a retention cap that is notched to correspond with two locator notches added to the worm gear.

All components [Fig. 5(c)] of the adjustable quarter-waveplate design must be entirely non-magnetic due to their close proximity to the sensing atoms within the sensor package. The worm gear and drive gear require the highest accuracy, robustness, and finest resolution, as the minimum tooth resolution is defined by the production method. These components are produced using titanium 3D printing (25 μm minimum print resolution) by a commercial supplier. The choice of titanium means wear and tear of the gear teeth is not a concern. The enclosure

and retention cap are 3D printed in Formlabs Grey Pro engineering resin (50 μm minimum print resolution).

2.2 Sensor Operation

The zero field magnetometer described here utilizes the Hanle effect to detect changes in the magnetic field on one axis, in the y-direction. The Hanle effect refers to the behavior of laser light passing through an atomic medium under the influence of a close-to-zero magnetic field. The response of light transmission to the magnetic field is directionally dependent on the static magnetic field, as described in Ref. 15. As part of the calibration routine, the zero-field magnetometer utilizes its directional sensitivity to detect and cancel static residual magnetic fields near the sensor in three axes, applying values of B_{x0}, B_{y0}, and B_{z0}, the magnetic field values required to cancel static residual fields in the environment.

The cancellation procedure is as follows: B_x, B_y, and B_z are swept in each axis in turn, while monitoring the transmission of light through the vapor cell. The transmission response measured by the PD voltage, A, with respect to the x- and z-axes is first measured, as shown in Fig. 6(a). At this point the values for B_{x0} and B_{z0} can be determined as the point at which the Lorentzian response in transmission along the x-axis is sharpest.

Once static residual fields are canceled on the x- and z-axes, a modulating field, B_{mod} is applied along the y-axis. The static field B_y on the y-axis may be swept, and by demodulating the resultant signal A_{Demod} at each value of B_y, a dispersive signal may be obtained, as shown in Fig. 6(b). This modulated Hanle resonance indicates the response that changing magnetic fields on the y-axis induce in the transmission signal after lock-in detection. The slope of the demodulated Hanle resonance allows the voltage from the PD to be converted into a measurement of the magnetic field. The zero-crossing point of this dispersive feature indicates the zero-field point on the y-axis.

After residual fields on each axis have been nulled by applying B_{x0}, B_{y0}, and B_{z0} and the sensor has been calibrated, the sensor may be operated in free-running mode. In free-running mode, the magnetic field is modulated on the y-axis, and the PD voltage is continuously monitored, as shown in Fig. 6(c), for changes in the magnetic field on the y-axis. After demodulation, this voltage may be scaled to units of magnetic field, and the time-varying magnetic field may be monitored.

The noise floor of the sensor is measured by operating the sensor in the free-running mode and analyzing the demodulated signal using the square root of the power spectral density (PSD). The power of the noise spectrum in the defined band of interest can be calculated to give a sensitivity figure of merit, in units of $\text{T}/\sqrt{\text{Hz}}$.

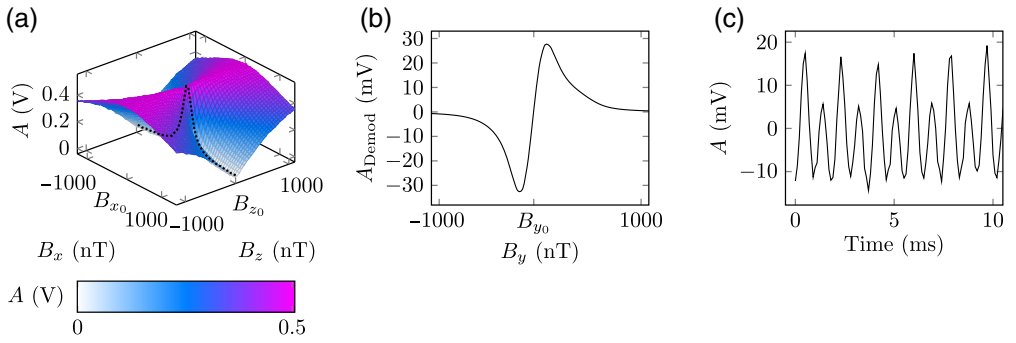

Fig. 6 Experimental signals arising from sensor operation. (a) Transmission of the light through the atomic vapor as a function of the applied field on the x- and z-axes. The narrowest point on this saddle-like landscape indicates the field values necessary to null the residual field. The peak transverse resonance at zero-field is indicated by the black dotted line. (b) The modulated Hanle response, a plot of demodulated voltage as a function of applied field on the y-axis. The slope of the linear region (mV/nT) may be used to convert from demodulated voltage to magnetic field units. (c) The free-running signal measured on the PD with respect to time.

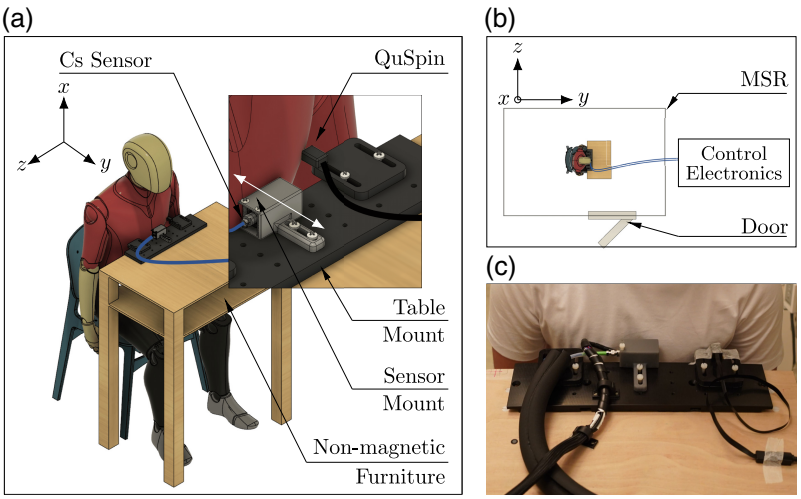

Fig. 7 Magnetocardiogram setup for the prototype cesium portable sensor. (a) The participant is seated on non-magnetic furniture with their chest close to the prototype sensor. A commercial sensor (QuSpin QZFM Gen-2) is mounted 10 cm from the prototype sensor. Inset shows both sensor locations, the sensitive axis of the prototype sensor (indicated with a white arrow) and the 3D printed table/ sensor mounts. (b) Participant with respect to MSR and sensor control electronics (housed external to MSR). (c) Photograph of participant leaning against the stationary sensors with the prototype sensor central with respect to their chest.

2.3 Magnetocardiography

To demonstrate the practical nature of the prototype sensor, a biomagnetic measurement was made in which the magnetic signal of the human heart was measured. Magnetocardiography (MCG) has gained research interest due to functional and clinical benefits pertaining to cardiac source location accuracy[35,36] in comparison to electrocardiography. MCG measurements with SERF OPMs have been widely used as a viable demonstration of OPM portability, sensitivity, and suitability for biomagnetic measurements for single[37] and multichannel systems.[32,33,38,39]

Figure 7 shows the MCG setup for the cesium portable sensor. A magnetocardiogram measurement from a human subject was taken. One participant took part in the study. The participant gave written, informed consent, and the study was approved by the University of Nottingham Medical School Research Ethics Committee. The MCG measurement took place inside an MSR (Vacuumschmelze Ak3b with two layers of MuMetal and one layer of copper). The experimental setup of the measurement of the MCG measurement is as follows: the participant to be measured sits within the MSR on non-magnetic furniture. The prototype cesium sensor is mounted to the non-magnetic furniture with 3D printed table and sensor mounts, shown in Fig. 7(a) inset. A commercial sensor (QuSpin QZFM Gen-2) is mounted 10 cm from the prototype sensor, to facilitate concurrent measurement for signal verification. The QuSpin has a sensitivity of $<15\ \mathrm{fT}/\sqrt{\mathrm{Hz}}$ in the band between 3 and 100 Hz. The participant placed their chest close to the stationary sensors to align with their approximate heart location, Fig. 7(c).

The portable sensor cabling, which comprises control signals, detection, and optical fiber were routed through a small hatch in the MSR. All control electronics are housed outside of the MSR, Fig. 7(b), including the laser driver, coil driver, transimpedance amplifier, heater driver, and data acquisition unit. Physically shielding the sensor from the driving electronics signals reduces the noise contributions and improves the sensitivity of the sensor.

3 Results

3.1 Skin Safe Sensor Operation

To test the requirement of a skin safe external sensor surface, the atomic vapor cell is ohmically heated to a set temperature of 120°C that is maintained for >90 min through closed-loop PID temperature control. The time period simulates sustained sensor operation. The temperature of the cell (T_{Cell}) and the external face of the sensor (T_{Outer}) are measured directly using two T-type thermocouples. Figure 8(a) shows measured temperature responses.

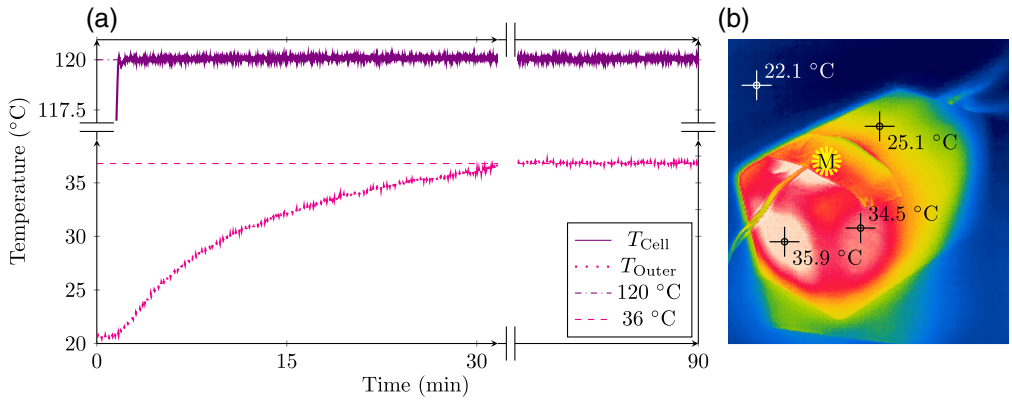

Fig. 8 Temperature measurement (via T-type thermocouple) of the portable cesium sensor for 90 min of cell heating, at desired cell temperature (120°C). (a) Measured temperature of cesium MEMS cell (T_{Cell}), (solid line) and external face of 3D printed case of the sensor T_{Outer}, (dotted). The measured cell temperature settling at the desired temperature is achieved through PID temperature control. Set temperature (dot-dashed) and saturation temperature of sensor external face (dashed). (b) Sensor external faces pictured with a thermal camera, color indicates temperature from coolest (blue) to hottest (red). The sensor measurement face, M, is indicated by the yellow star.

The PID heating system quickly reaches the cell set temperature in ∼100 s and maintains a consistent (±0.5°C) temperature throughout 90 min duration once the set temperature is reached. The tuned PID parameters achieve an overshoot of ≤0.5°C.

The sensor package's outer surface saturates at a temperature of 36°C, indicated by the pink dashed line in Fig. 8(a), within 30 min. Figure 8(b) shows the sensor external faces pictured with a thermal camera (Seek SKU: LW-AAA) where the hot-spots of the portable sensor's surfaces are indicated in red.

3.2 Portable Sensor Performance

The performance of the prototype portable sensor is demonstrated through sensor noise floor analysis and practical MCG. All operational parameters for the prototype sensor are optimized for sensitivity performance using the methods described in Ref. 15. The sensor has a flat frequency response to applied fields out to at least 250 Hz. The dynamic range of the sensor is defined by the full-width half-maximum of the Lorentzian response, here 174 nT, corresponding to a dynamic range of ±87 nT.

The sensitivity of the prototype sensor is measured through analysis of the magnetic noise floor. The noise floor is measured in a quiet shielded environment while no external signals are introduced. By measuring the magnetic field in this way over a 1 s interval, the inherent noise of the sensor may be assessed. This data are taken using a 16-Bit data acquisition (DAQ) at 1 MS/s, which is downsampled to 10 kS/s. The time series measurement is analyzed by taking the square root of the PSD, computed using a Hanning window, giving the noise floor of the sensor across a defined frequency band, seen in Fig. 9(a). A 1 s measurement interval is used here due to acquisition memory limits, but longer measurement intervals would lessen the effects of low frequency noise on the sensor. The optimized sensor sensitivity of 90 $\mathrm{fT}/\sqrt{\mathrm{Hz}}$ is defined as the geometric mean of the noise spectrum across the frequency band of interest (5 to 20 Hz).

The stability of the laser is characterized through direct measurement of the light polarisation over 12 h. The measured polarization at the output of the optical fiber is highly inconsistent, changing as much as $\simeq\pi/4$ rotation per hour. The polarization drift has a large impact on optical pumping efficiency, affecting the magnetic resonance amplitude and subsequently the sensitivity of the sensor.

The prototype cesium portable sensor has been successfully used for MCG, as shown in Fig. 9(b). The cardiac signal is resolvable in the prototype cesium portable sensor response after the application of a 1 to 40 Hz band-pass filter. The SNR of the prototype sensor signal is improved by averaging over 60 heart beats after triggering the signal with respect to the

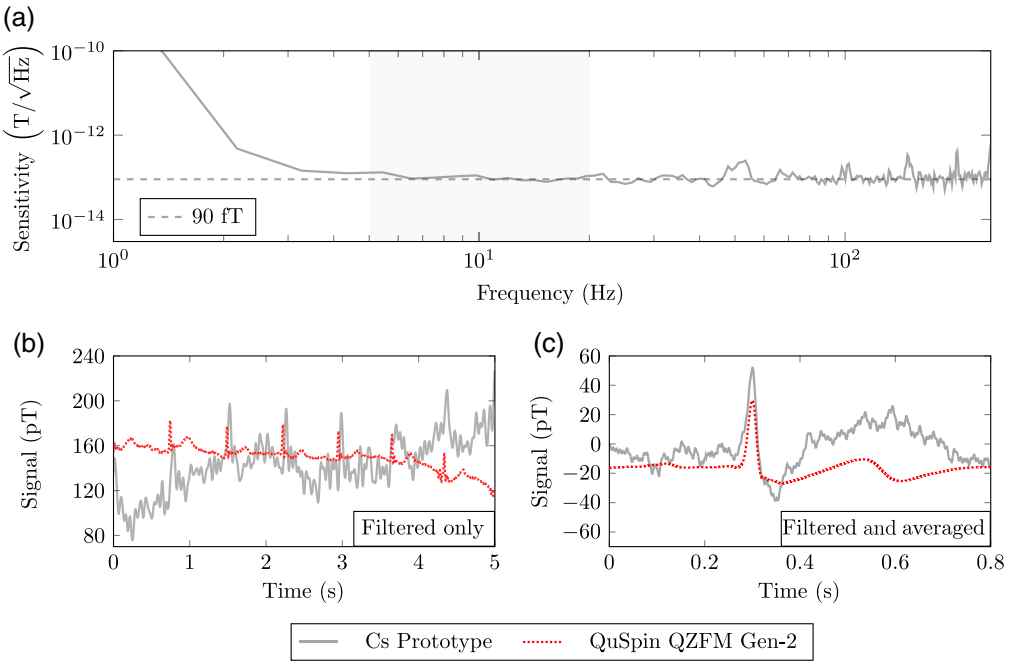

Fig. 9 (a) Measured magnetic noise floor of the sensor. The frequency band used to calculate sensitivity of the sensor is highlighted in gray. The dashed line indicates the geometric mean calculated in the frequency band of interest. This measurement was taken in a five-layer Mu-metal shield (Magnetic Shields Limited). (b), (c) Magnetocardiogram measured simultaneously using the portable cesium prototype sensor and QuSpin QZFM Gen-2 sensor inside an MSR, using a band-pass filter from 1 to 40 Hz on both responses. (b) Real-time responses of both sensors, without averaging. (c) Both responses averaged across 60 heartbeats.

QuSpin. It is likely that the laser and the fiber coupling the light to the sensor head contribute a large amount of uncorrelated noise to the measurement over the measurement window.

4 Discussion

We have presented the design of a prototype single-beam cesium portable sensor and proved its suitability for use in practical measurements through a demonstrated MCG measurement. Key miniature and microfabricated elements of a prototype portable sensor were presented and shown to have been successfully implemented.

The heating, temperature control, and insulation methods can maintain the required cell temperature for prolonged timescales (>90 min) while the package outer remains at skin safe temperatures (<37°C). This supports the use of these heating and insulation methods and also the use of cesium in this application due to lower heating requirements compared to other alkalis and subsequent lower external temperature.

Miniaturized bi-planar coils are implemented to provide three-axis fields with a very small footprint within the sensor, with a high degree of field homogeneity across the sensing area. Future improvements to the coil design will increase the field to current ratio of the coils, to allow for greater field control.

While the prototype portable sensor is larger than similar commercial sensors, there is scope for further miniaturization using many of the design techniques implemented here. Bi-planar PCB coils can be made for any future custom geometry in the same method as presented above. All 3D printed components (such as high temperature optical inserts) are designed and manufactured fully in-house and may be scaled down further as application-specific needs arise, including removal of the rotatable waveplate. It is expected that through optimization of individual package components, reductions up to 10% could be made on each external dimension. MEMS cell production also allows for custom geometry of cells and selection of required buffer gas pressures. The modular nature of the sensor allows for new optical configurations to be realized easily.

The cesium single beam prototype sensor has a peak sensitivity of 90 $\mathrm{fT}/\sqrt{\mathrm{Hz}}$, which is limited compared to leading commercial sensors.[9,23] Here, the limitations to sensitivity are predominantly due to laser instability. As such, future improvements include the reduction of common mode noise using differential measurement,[21,40] for which the sensor package has been designed. Transition to an on-package laser source such as a VCSEL would also aid in the reduction of optical noise, in particular as a way to mitigate noise introduced due to the optical fiber. Integration of the laser to an on-package configuration will improve the functionality of this device by allowing movement of the sensor while worn by a subject.

The prototype portable single-beam SERF sensor described here is a step toward the development of cesium-based SERF sensors that operate at a skin-safe temperature, with a compact footprint and sensitivity suitable for a range of biomagnetic measurements. This prototype sensor serves as a test-bed for novel and improved components, allowing further miniaturization and customization for specific biomagnetic signals.

Disclosures

M.J.B. is a director of Cerca Magnetics Limited, a spinout company whose aim is to commercialize aspects of OPM technology. N.H. holds founding equity in Cerca Magnetics Limited and sits on the scientific advisory board. Since completing the study M.R. has become an employee of Cerca Magnetics Limited.

Code and Data Availability

All data created during this research are openly available from Pure Data. DOI: https://doi.org/10.15129/8823c26c-1692-4824-9ac6-bf9a66af98db.

Acknowledgments

This research was funded by UKRI Grant No. EP/T001046/1. The authors would like to thank Rasmus Zetter for assistance with the bfieldtools software package.

References

1. A. Meyer-Baese et al., "A comprehensive review of magnetoencephalography (MEG) studies for brain functionality in healthy aging and Alzheimer's Disease (AD)," *Front. Comput. Neurosci.* **12**, 60 (2018).
2. R. König, C. Sielużycki, and P. J. Durka, "Tiny signals from the human brain: acquisition and processing of biomagnetic fields in magnetoencephalography," *J. Low Temp. Phys.* **146**, 697–718 (2007).
3. E. Boto et al., "Wearable neuroimaging: combining and contrasting magnetoencephalography and electroencephalography," *NeuroImage* **201**, 116099 (2019).
4. R. Hari and R. Salmelin, "Magnetoencephalography: from SQUIDs to neuroscience. Neuroimage 20th Anniversary Special Edition," *NeuroImage* **61**, 386–396 (2012).
5. H. B. Dang, A. C. Maloof, and M. V. Romalis, "Ultrahigh sensitivity magnetic field and magnetization measurements with an atomic magnetometer," *Appl. Phys. Lett.* **97**, 151110 (2010).
6. J. C. Allred et al., "High-sensitivity atomic magnetometer unaffected by spin-exchange relaxation," *Phys. Rev. Lett.* **89**, 130801 (2002).
7. M. P. Ledbetter et al., "Spin-exchange-relaxation-free magnetometry with Cs vapor," *Phys. Rev. A: At. Mol. Opt. Phys.* **77**, 033408 (2008).
8. J. Fang et al., "Optimizations of spin-exchange relaxation-free magnetometer based on potassium and rubidium hybrid optical pumping," *Rev. Sci. Instrum.* **85**, 123104 (2014).
9. M. J. Brookes et al., "Magnetoencephalography with optically pumped magnetometers (OPM-MEG): the next generation of functional neuroimaging," *Trends Neurosci.* **45**, 621–634 (2022).
10. B. U. Westner et al., "Contactless measurements of retinal activity using optically pumped magnetometers," *NeuroImage* **243**, 118528 (2021).
11. E. Boto et al., "On the potential of a new generation of magnetometers for MEG: a beamformer simulation study," *PLoS One* **11**(8), e0157655 (2016).
12. M. Rea et al., "A 90-channel triaxial magnetoencephalography system using optically pumped magnetometers," *Ann. N. Y. Acad. Sci.* **1517**, 107–124 (2022).
13. M. Jas, S. R. Jones, and M. S. Hämäläinen, "Whole-head OPM-MEG enables noninvasive assessment of functional connectivity," *Trends Neurosci.* **44**, 510–512 (2021).
14. E. Boto et al., "Moving magnetoencephalography towards real-world applications with a wearable system," *Nature* **555**, 657–661 (2018).

15. R. Dawson et al., "Automated machine learning strategies for multi-parameter optimisation of a caesium-based portable zero-field magnetometer," *Sensors* **23**, 4007 (2023).
16. S. Dyer et al., "Micro-machined deep silicon atomic vapor cells," *J. Appl. Phys* **132**, 134401 (2022).
17. T. Dyer et al., "Micro-fabricated caesium vapor cell with 5 mm optical path length," *J. Appl. Phys.* **132**, 204401 (2022).
18. J. F. Schneiderman, "Information content with low- vs. high-Tc SQUID arrays in MEG recordings: the case for high-Tc SQUID-based MEG," *J. Neurosci. Methods* **222**, 42–46 (2014).
19. M. J. Lewis, "Review of electromagnetic source investigations of the fetal heart," *Med. Eng. Phys.* **25**(10), 801–810 (2003).
20. Y. Wang et al., "Evaluation of optical parameters for a microminiature Rb vapor cell in a dual-beam SERF magnetometer," *Opt. Express* **30**(13), 23587–23599 (2022).
21. Y. Chen et al., "Single beam Cs-Ne SERF atomic magnetometer with the laser power differential method," *Opt. Express* **30**(10), 16541–16552 (2022).
22. K. Jensen et al., "Magnetocardiography on an isolated animal heart with a room-temperature optically pumped magnetometer," *Sci. Rep.* **8**, 16218 (2018).
23. S. Zahran et al., "Performance analysis of optically pumped 4He magnetometers vs. conventional SQUIDs: from adult to infant head models," *Sensors* **22**, 3093 (2022).
24. N. Holmes et al., "Balanced, bi-planar magnetic field and field gradient coils for field compensation in wearable magnetoencephalography," *Sci. Rep.* **9**, 14196 (2019).
25. M. S. Mrozowski et al., "Ultra-low noise, bi-polar, programmable current sources," *Rev. Sci. Instrum.* **94**, 014701 (2023).
26. J. Kitching, "Chip-scale atomic devices," *Appl. Phys. Rev.* **5**(3), 031302 (2018).
27. J. Fang et al., "Spin-exchange relaxation-free magnetic gradiometer with dual-beam and closed-loop Faraday modulation," *J. Opt. Soc. Am. B* **31**, 512 (2014).
28. J. Sheng et al., "Magnetoencephalography with a Cs-based high-sensitivity compact atomic magnetometer," *Rev. Sci. Instrum.* **88**, 094304 (2017).
29. M. C. D. Tayler et al., "Miniature biplanar coils for alkali-metal-vapor magnetometry," *Phys. Rev. Appl.* **18**, 14036 (2022).
30. A. J. Mäkinen et al., "Magnetic-field modeling with surface currents. Part I. Physical and computational principles of bfieldtools," *J. Appl. Phys.* **128**(6), 063906 (2020).
31. R. Zetter et al., "Magnetic field modeling with surface currents. Part II. Implementation and usage of bfieldtools," *J. Appl. Phys.* **128**(6), 063905 (2020).
32. Y. Yang et al., "A new wearable multichannel magnetocardiogram system with a SERF atomic magnetometer array," *Sci. Rep.* **11**, 5564 (2021).
33. R. Wyllie et al., "Magnetocardiography with a modular spin-exchange relaxation-free atomic magnetometer array," *Phys. Med. Biol.* **57**, 2619 (2012).
34. V. Shah and M. V. Romalis, "Spin-exchange relaxation-free magnetometry using elliptically polarized light," *Phys. Rev. A* **80**, 013416 (2009).
35. M. Nomura et al., "Noninvasive localization of accessory pathways by magnetocardiographic imaging," *Clin. Cardiol.* **17**, 239–244 (1994).
36. F. E. Smith et al., "Comparison of magnetocardiography and electrocardiography: a study of automatic measurement of dispersion of ventricular repolarization," *EP Europace* **8**, 887–893 (2006).
37. K. Kamada, Y. Ito, and T. Kobayashi, "Human MCG measurements with a high-sensitivity potassium atomic magnetometer," *Physiol. Meas.* **33**, 1063 (2012).
38. Y. J. Kim, I. Savukov, and S. Newman, "Magnetocardiography with a 16-channel fiber-coupled single-cell Rb optically pumped magnetometer," *Appl. Phys. Lett.* **114**, 143702 (2019).
39. O. Alem et al., "Fetal magnetocardiography measurements with an array of microfabricated optically pumped magnetometers," *Phys. Med. Biol.* **60**, 4797–4811 (2015).
40. D. Ma et al., "Analysis and measurement of differential-mode magnetic noise in Mn-Zn soft ferrite shield for ultra-sensitive sensors," *Materials* **15**, 8704 (2022).

Biographies of the authors are not available.